

Flow and electrical anisotropy in the upper mantle: Finite-element models constraints on the effects of olivine crystal preferred orientation and microstructure

Alexander Gatzemeier, Andréa Tommasi*

Lab. Tectonophysique, CNRS/Université de Montpellier II, F-34095 Montpellier Cedex 5, France

Received 1 August 2005; received in revised form 4 January 2006; accepted 25 January 2006

Period magnetotelluric (MT) data shows that electrical conductivity in the upper mantle is highly anisotropic. Agreement with electrical conductivity directions and seismic anisotropy fast directions suggests that anisotropic diffusion of hydrogenated olivine crystals controls the anisotropy of electrical conductivity in the upper mantle, since both seismic waves and diffusion are faster along the [1 0 0] axis of olivine. Thus, MT electrical anisotropy data, like seismic anisotropy, may be related to flow patterns in the upper mantle. However, observed electrical anisotropies are significantly higher than seismic ones. We study the influence of strain-induced crystal preferred orientations of olivine on upper mantle bulk electrical conductivities, using the macroscopic electrical conductivity anisotropy of a series of naturally and experimentally deformed peridotites in a finite-element model. These models, which fully take into account the microstructure: crystal and shape preferred orientations, based on orientation maps obtained by indexation of electron back-scattered diffraction (EBSD) patterns, show anisotropic electrical anisotropy factors ranging from 3 to 16. The intensity of electrical anisotropy depends to first order on the intensity of the olivine crystal preferred orientations, but the relation saturates for strong crystal preferred orientations. In addition, the spatial distribution of the various crystal orientations may significantly enhance influence the anisotropy in strongly deformed mantle rocks. The strongest anisotropy factors (>10) occur in mantle rocks in which deformation by dislocation creep is not only crystal but also strong shape preferred orientations, even if the latter is masked by recrystallization. Higher anisotropy factors (>100) observed in a few MT experiments imply however an additional, as yet unknown, mechanism controlling electrical anisotropy at asthenospheric depths in these regions. © 2006 Elsevier B.V. All rights reserved.

Keywords: Electrical conductivity; Mantle anisotropy; Hydrogen diffusivity; Lattice-preferred orientation; Finite-element modeling

Introduction

Period magnetotelluric (MT) data shows that electrical conductivity in the upper mantle, in particular the asthenosphere, is highly anisotropic.

Anisotropy factors (electrical anisotropy is defined as the ratio between highest and lowest electrical conductivity, $A = \sigma_{\max}/\sigma_{\min}$) obtained for sublithospheric depths (100–200 km) range from >2 beneath central Australia (Simpson, 2001) to >100 in Central Germany (Leibecker et al., 2002; Gatzemeier and Moorkamp, 2005). Different processes may produce this anisotropy: (1) aligned melt lenses resulting from partial melting at the lithosphere–asthenosphere boundary, (2) aligned

cting films (e.g., graphite or sulphides) along
aries, or (3) anisotropic diffusion of hydro-
ong oriented olivine crystals.

s by far the most abundant (~50–70 vol.%)
le mineral. As the principal interconnected
nductivity is assumed to dominate the bulk
y of the upper mantle down to the transition
km depth (Duba and Constable, 1993; Xu et
Moreover, agreement between electrical and
otropy fast directions in regions as varied as
le belt in Canada (Ji et al., 1996; Sénéchal et
ne Appalachians (Wannamaker et al., 1996),
ovince (Eaton et al., 2004), central Australia
001), and central Germany (Gatzemeier and
2005) suggests that seismic and electrical
have a common cause. Seismic anisotropy
r mantle is linked to coherent orientation of
tals over length scales of tens to hundreds of
n the upper mantle (Nicolas and Christensen,
price et al., 2000). Like the propagation of
es (or polarization for shear waves), H⁺ dif-
ter along the [1 0 0] axis of the olivine crystal
and Mackwell, 1990, Mackwell and Kohlst-
Thus, preferred orientation of olivine [1 0 0]
roduce electrical anisotropy in the astheno-

ents at high temperature and moderate pres-
ll as extensive data on naturally deformed
ks show that olivine at upper mantle con-
orms essentially by dislocation creep with
ip on the [1 0 0] (0 1 0) system, developing
al preferred orientations (CPO) characterized
nt of the [1 0 0] axis with the flow direction
[0 1 0] axis normal to the flow plane (see
ommasi et al., 2000). Thus, if H⁺ diffusion
the dominant electrical conductivity mech-
electrical conductivity directions map flow
n the asthenospheric mantle, similarly to fast
polarizations or fast P- or Rayleigh waves
directions. The high electrical conductivi-
t at asthenospheric depths (≥ 0.1 S/m) (e.g.,
t al., 1995; Simpson, 2001; Gatzemeier and
2005), which cannot be explained based on
al conductivity of dry olivine, provide evi-
dominant role of H⁺ diffusion in olivine in the
nduction at these depths (Hirth et al., 2000).
; in contrast to seismic anisotropy data,
ulk electrical anisotropies (Simpson, 2003;
and Moorkamp, 2005) are significantly

tion. A fundamental parameter to this question is how the
electrical anisotropy produced by anisotropic H⁺ diffu-
sion in individual olivine crystals is transferred to the
polycrystal (rock) scale.

In this article, we use finite-element modelling
(Garboczi, 1998) to evaluate macroscopic electrical
anisotropy associated with intracrystalline diffusion of
H⁺ in olivine in three naturally deformed peridotites
and a synthetic dunite deformed in simple shear at
high temperature and pressure. These models fully
take into account the microstructure of the rocks: both
crystal and shape preferred orientations are explic-
itly described based on orientation maps obtained by
indexation of electron back-scattered diffraction (EBSD)
patterns. Predicted anisotropies are then compared (i)
to anisotropies predicted by simple averaging models
(Voigt–Reuss–Hill), which are traditionally used to cal-
culate seismic and thermal properties of upper mantle
rocks (e.g., Ben Ismail and Mainprice, 1998; Tommasi
et al., 2001), and by random resistor networks (Simpson
and Tommasi, 2005) and (ii) to electrical anisotropies
inferred from long period MT data.

2. Modelling electrical properties of composite media

The prediction of effective electrical properties of
composite media from the properties and microstruc-
ture of its components has applications in many areas,
from material sciences to geophysics (e.g., Archie, 1942;
Schmelting, 1986; Coverdale et al., 1995). A large num-
ber of approaches may be used to obtain the electrical
conductivity of a composite. In the absence of infor-
mation on texture, effective medium theory using sim-
ple conduction models can be applied to obtain bulk
electrical properties of the composite. These models
describe heterogeneous, two-phase materials where a
phase of often high electrical conductivity is embed-
ded into a low-conductive, interconnected matrix. The
effective conductivity of such medium is dependent not
only of the electrical conductivity of the constituents,
but also on their volume fraction, geometry and inter-
connectivity. The simplest mixing models are the series
and parallel models (e.g., Schulgasser, 1976). In reality,
neither of them is able to describe precisely the mix-
ture of materials. More complex and realistic expressions
describing the conductivities of mixtures with isolated
high conductivity phases have been developed, like the
Maxwell (1881) model for isolated conducting spheres

ions on a two-phase mixture are given by and Shtrikman (1962) model. Other results, Landauer's (1952) effective medium theory, Del Rio et al., 2005's effective conductivity (Del Rio et al., 2005) for two-phase 2D materials, or the simple geophysical model (Shankland and Duba, 1990), lie between the two bounds. An effective-medium model for a mixture with phases of anisotropic conduction was derived by Bernasconi (1974). Extending Landauer's (1952) effective-medium approximation to mixtures with different conductivity distributions in the orthogonal directions, this approach allows for calculating effective conductances in three orthogonal directions. A further extension allows describing more complex microstructures (Toledo et al., 1992).

Percolation theory describes how a phase percolates in a mixture, i.e., if it is sufficiently connected along the entire model, it has a significant influence on the overall properties (Landauer, 1952; Kirkpatrick, 1973). In this case, effective medium theory assuming a homogeneous distribution becomes percolation theory (Guéguen and Palciauskas, 1994). Percolation theory and renormalization methods describe the conductivity of so-called clusters, i.e., areas with specific properties, on networks with extreme contrast in the physical properties of their constituents (Kirkpatrick and Aharony, 1992). These methods allow for calculating the conductance of networks with statistical distribution of open or connected bonds. Random resistor networks (e.g., Madden, 1976; Bahr, 1997) or fractal networks (Bigalke, 1999) have been successfully used to calculate electrical conduction of heterogeneously distributed phases. For modelling anisotropic conductivity, Landauer (1952) combined effective medium and percolation theory by introducing a topological parameter: the connectivity.

These methods have been used to model electrical conductivities of crustal and mantle rocks under various conditions (e.g., Shankland and Waff, 1977; Jödicke, 1999; Sidze et al., 1999; Roberts and Tyburczy, 1999; 2000b). For the upper mantle, most studies compare anisotropic conductivities described by (i) a single phase system dominated by the electrical conductivity of dry olivine (e.g., Constable et al., 1992; Duba et al., 1993; Xu et al., 2000b) or (ii) a two-phase system with dry olivine as a matrix with an embedded conductive phase, like partial melt (e.g., Roberts and Tyburczy, 1999). Indeed, olivine, which is by far the most abundant upper mantle mineral, shows little electrical conductivity under dry conditions: the largest and smallest

electrical conductivity may be described as isotropic, even in presence of strong olivine lattice preferred orientations.

On the other hand, under high temperature and hydrated conditions, electric conduction in the upper mantle is dominated by H⁺ diffusion in olivine (Karato, 1990). According to the Nernst–Einstein equation, which relates ionic conductivity to charge carrier concentration and mobility, conductivities are proportional to diffusivities of the charge carrying species:

$$\sigma_i^{\text{H}^+} = \frac{f c_{\text{H}^+} D_i q^2}{k_B T}, \quad (1)$$

where $\sigma_i^{\text{H}^+}$ is the electrical conductivity, f a numerical (correlation) factor approximately equal to unity, c_{H^+} the concentration (m⁻³), D_i the diffusivity along direction i and q is the electrical charge of the charged species (Karato, 1990). Hydrogen diffusion in single crystal olivine is fast and highly anisotropic ($D_{[100]} \approx 20D_{[010]} \approx 40D_{[001]}$, Kohlstedt and Mackwell, 1998). This conduction mechanism leads therefore to high electrical conductivity and anisotropy at the crystal scale and, if these properties are preserved at the polycrystal and larger scales, high conductivity and anisotropy in the upper mantle (e.g., Lizarralde et al., 1995; Simpson, 2003; Gatzemeier and Moorkamp, 2005).

To evaluate the bulk electrical conductivity anisotropy that may result from anisotropic H⁺ diffusion in the upper mantle, Simpson and Tommasi (2005) developed a model based on random resistor networks that accounts for realistic upper mantle mineralogical compositions, crystal preferred orientations, and rates of H⁺ self-diffusion in olivine and pyroxenes. This model predicts a mean electrical anisotropy factor less than 3 for a peridotitic mantle. However, this model, as all methods described above, does not take into account the microstructure of the samples.

3. FEM modelling of effective electrical conductivities of polycrystalline aggregates

In a 3D finite-element model (FEM), the effective electrical conductivity tensor of a polycrystalline aggregate depends on the full microstructure, i.e., on the orientation and shape of the crystals that compose the aggregate, on their spatial distribution, and on their electrical conductivity tensors. The microstructural informa-

the orientation of the crystallographic lattice in the macroscopic reference frame. Each grain is defined by a set of neighbouring pixels with similar composition and orientation; a grain may be defined by a set of a few hundred pixels, depending on the resolution of the EBSD data. The crystal orientation data is used to orient the electrical conductivity tensor of each pixel. Bulk electrical conductivity of the aggregate are then obtained using finite-element modelling (FEM) by calculating the current densities that are produced by a constant current density (Garboczi, 1998).

The procedure employed in this study to obtain the electrical anisotropy for a given polycrystalline aggregate is divided into the following steps:

(1) The composition of the polycrystalline aggregate and the orientation of the individual grains is determined. Starting from thin sections of naturally or experimentally deformed mantle rocks, the mineral structure and CPO are determined by crystallographic orientation mapping using the electron-backscattered diffraction (EBSD) approach, in which the orientation of the crystal lattice relative to the macroscopic reference frame is obtained by the analysis of electron-backscattered diffraction patterns obtained with a scanning electron microscope. Each pixel in the EBSD map contains therefore information on the mineral phase and on the orientation of the crystal lattice of the grain it belongs to, given as Bunge–Euler angles (Bunge, 1982). In the present study we use EBSD data obtained from 2D thin sections, but this method can be applied for 3D blocks of material imaged by 3D-EBSD.

(2) The orientation mapping and indexing are performed automatically, the EBSD map contains information from misinterpreted diffraction patterns or noise due to fractures in the sample. Noise-reduction algorithms are used for cleaning the map of isolated pixels (spikes) that differ in composition or orientation from their nearest neighbours. The orientation of the pixels not indexed to these points is compared to the orientation of its eight nearest neighbours and replaced by the orientation of the neighbour that displays the minimum indexing error in the EBSD map. A similar procedure is used to fill up the gaps, i.e., areas where the determination of the crystal orientation from the diffraction pattern was not possible. For the filling procedure a minimum of five neighbouring pixels is imposed. Small orienta-

(3) In step 3, each mineral phase of the EBSD map is associated with a diagonal electrical conductivity tensor, the elements of which contain the conductivities along the main crystallographic axes. Depending on the mineral phase and Bunge–Euler angle of each pixel, the single crystal conductivity tensor is rotated into the macroscopic reference frame (XYZ of the model) and assigned to the element. In this way a two- or, in cases using 3D-EBSD data, a three-dimensional model is obtained that has in each point a 3D electrical conductivity tensor, which is a function of the local composition and crystallographic orientation.

(4) In step 4, the electrical anisotropy of the conductivity model is calculated using the finite-element code *elecsem3d* (Garboczi, 1998). As input files the program expects a 3D digital image consisting of cubic pixels in which each pixel can have a different phase characterized by an arbitrary symmetry conductivity tensor. The size of the digital image can vary in each direction and is limited only by the available computational resources. Periodic boundary conditions are applied to avoid influence on the calculation from the sample limits (*end effect*, Nye, 1985). These boundary conditions imply that the sample is representative for a larger region and hence that the model may be extended by repeating periodically the input digital image. In this paper we use digital images obtained from thin sections, and hence a 2D microstructure, but tensor (3D) conductivity properties. Extending the model along z direction via periodic boundary conditions results in a 3D conductivity model with a microstructure invariant along z-direction. For an applied (external) electric field $\vec{E}^{\text{ext}} = (E_x, E_y, E_z)$ the program calculates the resulting average current density $\vec{j}^{\text{ext}} = (j_x, j_y, j_z)$. These current densities are related to the electrical field by the effective electrical conductivity tensor

$$\vec{j}^{\text{ext}} = \sigma^{\text{eff}} \vec{E}^{\text{ext}}. \quad (2)$$

For an effective conductivity tensor with orthorhombic symmetry (diagonal form if x, y, z are main crystallographic axes) $\sigma^{\text{eff}} = j_i/E_i$ returns the main effective electrical conductivities. The electrical anisotropy as the ratio between the conductivities along two (orthogonal) directions follows as $A = \sigma^{\text{eff}}_i/\sigma^{\text{eff}}_j = j_i E_j / j_j E_i$.

Comment: The last step, transferring the currents to

lement program. In the general case, the bulk conductivity tensor of an aggregate, which is composed of crystals with orthorhombic tensor properties, is not orthorhombic but triclinic, resulting in six independent coefficients. However, for olivine the bulk conductivity tensor has a simpler form and can be approximated by an orthorhombic symmetry. In this case, alignment of the macroscopic coordinate system with the CPO results in small off-diagonal elements, and the electrical currents calculated along j_x, j_y can be directly used to obtain approximated electrical conductivities. The models presented in this study fulfil this condition, since the EBSD maps were performed on sections parallel to the flow direction and normal to the CPO plane, which contain the maximum concentration of olivine both the $[1\ 0\ 0]$ and $[0\ 1\ 0]$ crystallographic directions. In the general case, a set of numerical models with different sample orientations (≥ 6) is required to determine the six independent coefficients of the triclinic conductivity tensor (Nye, 1985). A full 3D model is then required. We are currently working on this issue.

Measuring electrical conductivity anisotropy in mantle rocks

Following the method described in the previous section, we investigate the influence of hydrogen diffusion on mantle electrical conductivity and anisotropy in four mantle peridotites with varying microstructures and olivine CPO. In this paper, speaking the electrical conductivity is the result of the conduction of all charge carriers: $\sigma = \sum \sigma_i$. In this study, since the mechanisms active in mantle rocks, we consider only conduction due to hydrogen diffusion. In the presence of water, it is assumed to dominate the electrical conductivity (e.g., Gatzemeier and Moorkamp, 2004).

In this study, we use hydrogen diffusivities along the crystallographic axes based on results of Mackwell and Kohlstedt (1990) and Kohlstedt and Mackwell (1998):

$$\begin{aligned} 10 \times D_{[0\ 0\ 1]}^{\text{ol}} &\approx 100 \times D_{[0\ 1\ 0]}^{\text{ol}} & (\text{MK90}) \\ 20 \times D_{[0\ 1\ 0]}^{\text{ol}} &\approx 40 \times D_{[0\ 0\ 1]}^{\text{ol}} & (\text{MK98}) \end{aligned} \quad (3)$$

Hydrogen diffusion is also anisotropic in Mg-rich olivines (Stalder and Skogby, 2003) with diffusivities intermediate between those along olivine $[0\ 1\ 0]$ axes:

According to Eq. (1) electrical conductivity depends not only on hydrogen diffusivities but also on hydrogen concentration. Water concentration in the upper mantle is still controversial and absolute value for the electrical conductivities due to H^+ diffusion cannot be obtained. However, anisotropy A is given by the ratio between the electrical conductivity in two orthogonal directions. According to Eq. (1), if hydrogen concentration is assumed to be the same in all crystals, the anisotropy does not depend on the hydrogen concentration, but only on the ratio between the diffusivities in the two directions

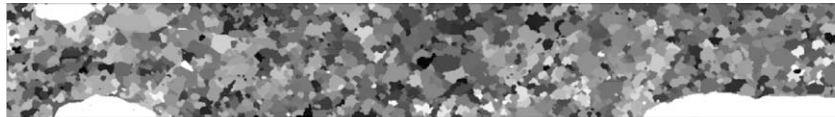
$$A = \frac{\sigma_i}{\sigma_j} = \frac{D_i}{D_j} \quad (5)$$

We assume identical hydrogen concentrations in all crystals. Therefore, olivine and enstatite conductivity tensors can be normalized by $\sigma_{[1\ 0\ 0]}^{\text{ol}}$, the electrical conductivity due to H^+ diffusion in olivine along the olivine $[1\ 0\ 0]$ axis. The resulting electrical conductivity tensors contain electrical conductivities relative to $\sigma_{[1\ 0\ 0]}^{\text{ol}}$, without further requirement about absolute water content in the minerals. Using these normalized conductivities allows to calculate bulk electrical conductivities (relative to $\sigma_{[1\ 0\ 0]}^{\text{ol}}$) and anisotropies of the sample.

4.1. Sample descriptions

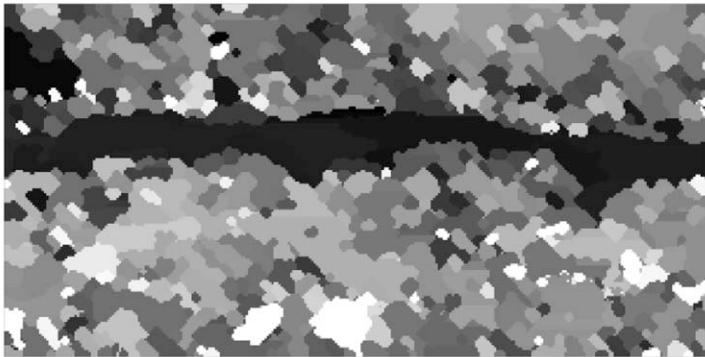
The studied samples are three naturally deformed peridotites and a synthetic dunite deformed in simple shear at high temperature and pressure. The selected samples have olivine contents (85–100%) that are significantly higher than typical asthenospheric mantle compositions (50–70% olivine), because the aim of the study is to evaluate the effect of the intrinsic anisotropy of H^+ diffusion in olivine and of the olivine preferred orientations on the macroscopic electrical anisotropy. The studied peridotites display a wide range of microstructures (variations in grain size and shape, Fig. 1) that allows testing the effect of the microstructure on the electrical conductivity.

EPTA3 is a dunitic xenolith (>95% olivine) from the Torre Alfina volcanic field in the Apennines (Italy) that shows a coarse-grained microstructure, characterized by mm-scale anhedral olivine grains (1–10 mm); the larger grains show widely spaced subgrain boundaries normal to the grain elongation (aspect ratio 2:1). This microstructure, characterized by a very weak shape



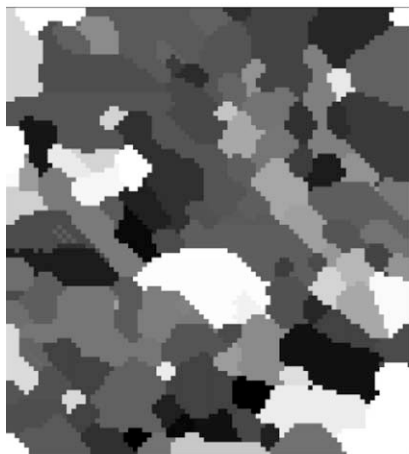
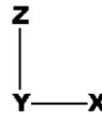
FRB1359

3mm = 200 steps



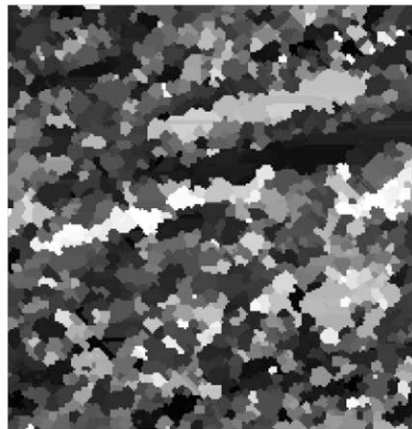
900A87

50 μm = 50 steps



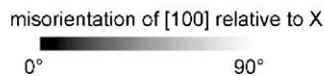
EPTA3

2mm = 20 steps



PO342

25 μm = 50 steps



EBSD orientation maps obtained by indexation of electron backscattered diffraction (EBSD) patterns for the four studied peridotites. The grayscale indicates the angular misorientation of the olivine [100] axis relative to the X direction, which corresponds to the lineation (maximum grain elongation) in the naturally deformed peridotites FRB1359 and 900A87, and to the extension direction in harzburgite 900A87, and to the shear direction in dunite PO342. All maps were performed in the XZ structural plane, parallel to the flow direction and normal to the flow plane.

900A87 is a harzburgitic xenolith (82% olivine, 15% pyroxene, 3% garnet) from the Premier Mine in South Africa. This sample is a high-strain mylonite, which shows an almost fully recrystallized and highly re-equilibrated microstructure,

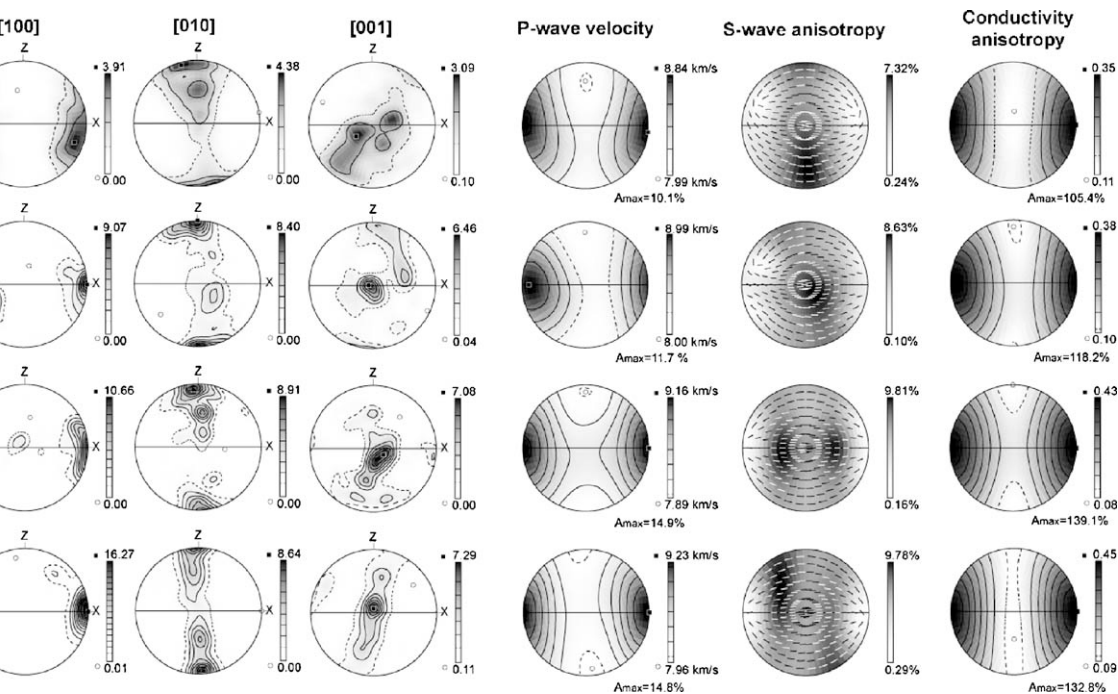
partially recrystallized olivine porphyroclasts are locally preserved. Enstatite occurs as cm-scale porphyroclasts elongated parallel to the foliation with very fine-grained recrystallization tails (<20 μm). The elongation of the olivine and pyroxene porphyroclasts and the alignment

temperature conditions ($T > 1400^\circ\text{C}$, Boullier and 075). The EBSD map used as the input for the s performed in a domain composed essentially allized polygonal olivine grains.

7 is a fine-grained mylonitic harzburgite (75% # = 91; 20% opx; 3% cpx; 2% sp) collected in low-temperature mylonitic zone in the Wuqba the Oman ophiolite that was further experimen- med in extension at 1200°C and 300 MPa at e of 10^{-5} s^{-1} (Ben Ismail, personal commu- t shows a well-developed lineation parallel to ion direction marked by the shape-preferred of olivine porphyroclasts (aspect ratios up and the orientation of fined-grained olivine-, respectively. Olivine porphyroclasts are up long and show undulose extinction, closely 00) subgrain walls, and irregularly shaped daries. Enstatite porphyroclasts are up to 1 cm e average grain size is 2–4 mm. The recrystal- x, which is mainly composed by olivine grains m in diameter, represents more than 70% in the sample. EBSD mapping was performed

in a domain devoid of enstatite with the X-axis parallel to the imposed extension direction.

PO342 is a synthetic dunite (100% olivine) deformed in simple shear at 1200°C and 300 MPa at a strain rate of $6 \times 10^{-5}\text{ s}^{-1}$ up to a shear strain of 5 (Bystricky et al., 2000). It is composed by a very homogeneous recrystallized matrix (95% volume) composed by $3\text{ }\mu\text{m}$ -wide equant or slightly elongated grains that surround two types of porphyroclasts. The first is formed by highly elongated ribbon grains (e.g., the black crystal that crosscuts the upper right domain of the EBSD map, Fig. 1) that are in an orientation for easy slip on (0 1 0) [1 0 0]. Their aspect ratios, which may attain 1:25, are consistent with the finite strain imposed to the sample. The second type of porphyroclasts (white in the map, Fig. 1) show lower aspect ratios (1:10), more subgrains and deformation features, and have an oblique lattice orientation. Both types of porphyroclasts have average grain areas equal to those of the starting grains (equivalent diameter of $20\text{ }\mu\text{m}$), suggesting that their shapes are due entirely to strain by dislocation glide. EBSD mapping was performed in a thin section secant to the cylinder within



the crystal preferred orientations and three dimensional distributions of P-wave velocity, S-wave polarization anisotropy, and electrical conductivity calculated by Voigt–Reuss–Hill averaging for the four studied peridotites. Electrical conductivity is calculated using the olivine H⁺ (Kukushkin et al., 2004; Knapik et al., 1999). For the anisotropy calculations, the X-axis is the extension direction and Z the direction of

n to its outer edge, the X-axis is parallel to
direction.

bles show olivine crystal preferred orienta-
(Fig. 2) characterized by a strong concen-
[1 0 0] parallel to the flow direction (inferred
the lineation in the EPTA3 and FRB1359,
tension or simple shear direction in 900A87
respectively). The [0 1 0] direction is aligned
the flow plane, with some dispersion in a
al to the flow direction in all samples except
3. These CPO are typical of deformation
ion creep under high temperature condi-
cterized by activation of $[100]\{0kl\}$ sys-
dominant glide on the (0 1 0) plane (Fig. 2).
O intensities vary from sample to sample
359 displaying the weakest orientation and
strongest. The intensity of a CPO may be
ed by the integral of the orientation distri-
tion, the J factor, which varies from 1 for
e aggregate to infinity for a single crystal
(32). Naturally deformed mantle rocks show J
een 2 and 30, but J factors higher than 18 are
a few dunites displaying abnormal growth,
0% of the studied peridotites displaying J fac-
n 3 and 14 (Tommasi et al., 2000). J factors
ed peridotites range from 4.75 for FRB1359
O342. The peridotites selected for this study
efore the entire range of CPO intensities used
in upper mantle rocks.

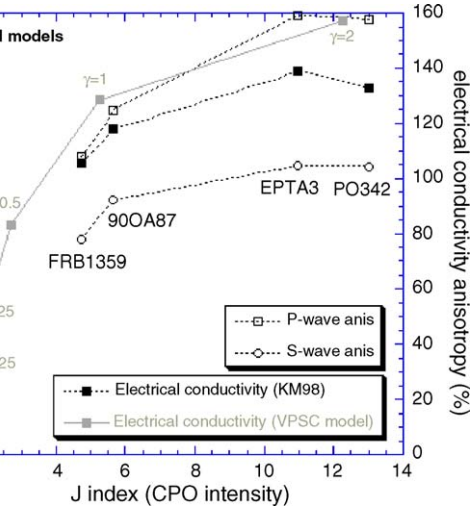
aint on the intrinsic anisotropy of a man-
e may be obtained by the analysis of the
c properties and electrical conductivity ten-
ed by simple volumetric averaging methods,
gt–Reuss–Hill (VRH) average (Hill, 1952),
e average of the parallel (Voigt, 1928) and
s, 1929) solutions (Mainprice and Humbert,
seismic properties, such an average, which
s to a random distribution of the various ori-
ponents, produces correct estimates of the
otropy, because seismic properties depend
on the mineralogical composition and on the
). Electrical conductivity, on the other hand,
o on the spatial distribution of the different
. The Voigt–Reuss–Hill (VRH) averaging
erefore a first approximation to the CPO-
ctrical anisotropy, which does not consider
f the microstructure. Discrepancy between
ge and FEM anisotropy indicates the influ-
nectivity of the high-conductivity phase on

aging based on the mineral composition and on the
CPO of the studied peridotites are shown in Fig. 2.
For better comparison between maximum seismic
and electrical anisotropies we define, in addition to
the usual electrical anisotropy factor, which is the
ratio between the maximum and minimum conduc-
tivities, a second electrical anisotropy measure, A_{\max}
(%) = $(\sigma_{\max} - \sigma_{\min}) \times 100 / \sigma_{\text{mean}}$. Maximum electrical
conductivities, like maximum P-wave velocities and the
polarization direction of the fast S-waves are parallel to
the concentration of [1 0 0] axis of olivine and, hence, to
the flow direction. Low conductivities and P-wave veloc-
ities are observed in a plane normal the flow direction,
with a weak minimum parallel to the maximum con-
centration of the [0 1 0] axis of olivine, i.e., normal to
the flow plane, in those samples for which olivine CPO
has an orthorhombic symmetry (EPTA3 and 900A87).
However, for EPTA3 and 900A87, conductivities and
velocities within the flow plane normal to the flow direc-
tion in the flow plane (in the Y direction of the structural
frame) are also very low. This suggests that strong elec-
trical conductivities anisotropies will be sampled for
all measurements including the flow direction, independ-
ently of the plane considered.

Seismic anisotropy for both P- and S-waves does
not display a linear dependence on CPO intensity, but
a fast increase of anisotropy at low J factors and sta-
bilization at J factors higher than 8 (Ben Ismail and
Mainprice, 1998). Electrical anisotropies obtained from
VRH averages reveal a similar dependence (Fig. 3). Cal-
culated electrical anisotropies range from 105.4% for
the FB1359 ($J=5$) to 139.1% for EPTA3 ($J=10$). PO342
that has the strongest CPO ($J=13$) shows a slightly lower
electrical conductivity anisotropy (132%).

4.2. FEM results

The finite-element modelling evaluates the current
densities along the sample coordinate axes x , y , z for
an applied electric field $E=(1, 1, 1)$. Current densities
and electrical field are related via the electrical conduc-
tivity tensor (Eq. (2)). Since a detailed description of the
microstructure is only available for the XZ plane (2D)
and the extension of the model in the third dimension
is ensured essentially by the periodic boundary condi-
tions, we only consider the current densities in the x and
 y directions. Comparing anisotropies of 2D and 3D ran-
dom resistor networks, Labendz (1999) only observed
dependence on models' dimension and intrinsic electri-



...ic ($A_{\max} (\%) = (V_{\max} - V_{\min}) \times 100 / V_{\text{mean}}$; open sym-
 ...H electrical ($A_{\max} (\%) = (\sigma_{\max} - \sigma_{\min}) \times 100 / \sigma_{\text{mean}}$; full
 ...) anisotropies as a function of the CPO intensity, mea-
 ... J index, of the studied samples. For comparison, the
 ...al conductivity anisotropy of a 100% olivine aggregate
 ... evolution of the CPO in simple shear is modelled by the
 ... self-consistent approach (Tommasi et al., 2000) is shown
 ... s. A better organization of the [1 0 0] axes in the modelled
 ... sults in slightly higher anisotropy at a given J index.

...ws current flow in the third spatial direction.
 ...odel, within plane anisotropies are therefore
 ... (or equal) than in an equivalent 2D model. In
 ... models, we use tensor electrical conductivi-
 ... aluate current densities in 3D, but the periodic
 ... conditions result in elongated grains along the
 ... that do not reflect sample geometry. How-

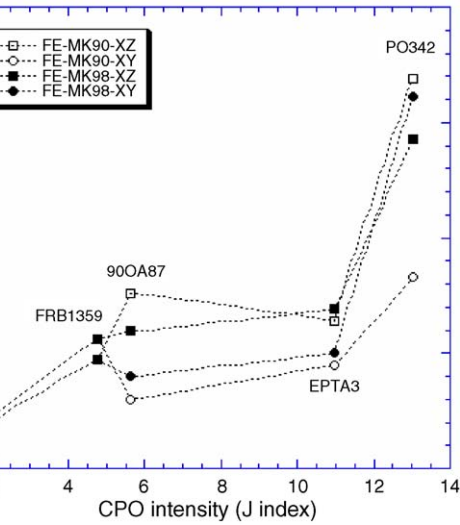
ever, all samples show similar and strong LPO. Thus, as far as grain boundaries are not the dominant charge carriers, the discrepancy between anisotropy in the x - y plane in the present 2.5D models and in a full 3D model is expected to be small. Electrical conductivity anisotropy is thus calculated as the ratio between the current densities along x and y direction as given in Step 4 for models using either the MK90 or the KM98 olivine H^+ diffusivity tensor (Eq. (3)).

Magnetotelluric (MT) data provide information about depth-dependence of horizontal electrical conductivities. Thus, MT data only provides constraints on the electrical anisotropy within the horizontal plane. Orientation maps were obtained in thin sections cut perpendicular to the foliation (flow plane which normal is the Z structural direction) and parallel to the lineation (flow or X structural direction). The models evaluate the anisotropy in this plane, for which the microstructure is fully described. They may be used therefore to estimate the horizontal electrical anisotropy in a vertical shear zone, in which both the flow direction and the normal to the flow plane are horizontal. To estimate the horizontal electrical anisotropy that would be produced in a horizontal shear zone, like the one that would form in the asthenosphere by viscous drag in response to the plate motion (Tommasi, 1998), we need to calculate the anisotropy within the flow plane. To evaluate this anisotropy, we run a second series of models in which we assume that (i) the microstructure (grain shapes and orientation spatial distribution) in the flow plane is similar to the one in the plane normal to the foliation that was analyzed by EBSD mapping and (ii) the CPO is rotated

...red orientations intensities (J factor), Voigt–Reuss–Hill (VRH), and finite-element (FEM) electrical anisotropies of the studied samples

J	Electrical anisotropies			
	VRH		FEM ($j_x/j_y/j_z/A$)	
	MK90	KM98	MK90	KM98
5.62	4.8	4.4	0.528/0.069/0.199/7.6	0.496/0.083/0.174/6.0
4.75	3.8	3.4	0.376/0.080/0.122/4.7	0.342/0.061/0.092/5.6
10.98	6.7	5.5	0.374/0.058/0.144/6.4	0.358/0.052/0.111/6.9
13.03	6.0	5.4	0.561/0.033/0.133/16.9	0.492/0.0343/0.111/14.3
5.62	3.4	3.3	0.521/0.173/0.082/3.0	0.451/0.113/0.095/4.0
4.75	2.7	2.8	0.408/0.073/0.086/5.6	0.335/0.072/0.109/4.7
10.98	3.2	3.5	0.433/0.096/0.048/4.5	0.353/0.070/0.062/5.0
13.03	4.8	4.5	0.497/0.061/0.048/8.3	0.419/0.026/0.045/16.1

...s ($A = \sigma_{\max} / \sigma_{\min}$) were calculated from the CPO and mineralogical compositions obtained from the crystallographic orientation maps
 Fig. 1. Electrical anisotropies were calculated using olivine H^+ -diffusivity tensors from Mackwell and Kohlstedt (1990) [MK90] and
 Mackwell (1998) [KM98]. For the FEM, we show the electric currents j_x, j_y, j_z and anisotropies $A = j_x/j_y$ that result from an applied



Electrical anisotropy factors in the XZ plane (normal to the foliation) and XY plane (within the foliation, circles) calculated from modelling using MK90 (empty symbols) and KM98 for the different samples as a function of the olivine (J index).

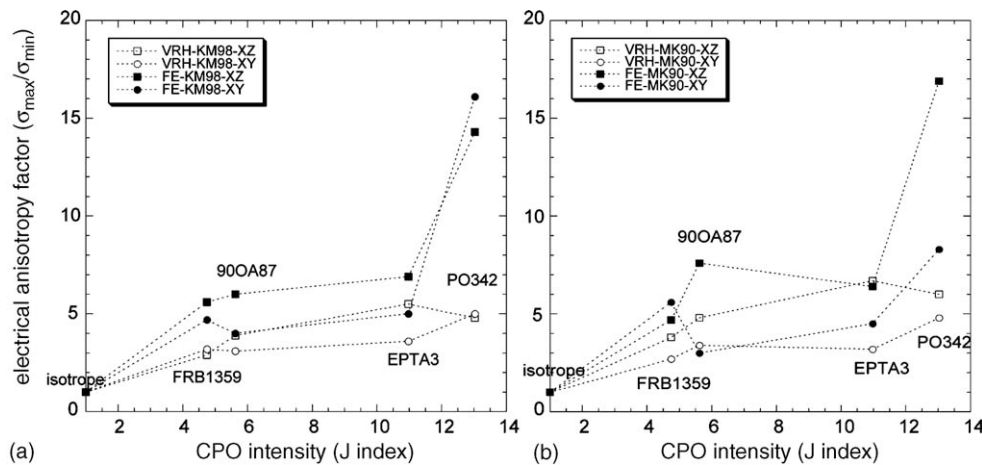
and the X macroscopic axis. Results for these “within the flow plane” models are indicated in Table 1.

Electrical conductivity in all models is parallel to X (Table 1). With exception of dunite PO342 that displays very strong anisotropy (attaining up to 16.9), anisotropy factors range between 3 and 8 and display a dependence on the CPO intensity (Fig. 4). This anisotropy is much weaker than the one observed in VRH

models, is better observed in models that evaluate the anisotropy in the XZ plane (normal to the foliation) using KM98 H⁺ diffusivity data. In this dataset, anisotropy factors vary between 5 and 7 for samples FRB1359 (J = 5) and EPTA3 (J = 11), respectively.

Anisotropy factors calculated for the XY plane, i.e., within the flow plane, are usually lower than those obtained in the XZ plane, but the difference is usually small and the trend may be even reversed for those samples displaying a strong dispersion of [0 1 0] and [0 0 1] normal to the flow direction, like PO342 or FRB1359. Calculated anisotropy factors do not differ significantly for models using MK90 or KM98 H⁺ diffusivity data in spite of the significant lower intrinsic anisotropy of the olivine crystal of the latter data, which has a single crystal anisotropy factor of 40 instead of 100 (Fig. 4). However, models using MK90 data tend to display a stronger difference between the anisotropies observed within and normal to the flow plane.

A comparison of VRH and FEM results show that FE electrical anisotropy factors systematically exceed the VRH ones, except for sample 900A87, for which FEM and VRH models using MK90 diffusivity data give similar results in the XZ plane (Fig. 5). VRH models should thus provide good lower bound estimations of upper mantle electrical anisotropies. In general the FEM results confirm the tendency observed for the VRH averages of increasing electrical anisotropy with increasing CPO intensity. However, the FEM results show that the spatial distribution and, hence, the interconnectivity of the various CPO components can significantly enhance the electrical anisotropy.



(a)

(b)

er analysis of the FEM results for samples
 1 900A87 highlights the effect of these two
 on the electrical anisotropy:

anisotropies calculated for sample PO342 are
 and those predicted by the VRH model. Indeed,
 3 and PO342 show a weak variation in J -
 that leads to similar values for P-, S-wave,
 VRH electrical anisotropies (Fig. 2), but dif-
 ferences in their FE electrical anisotropies
 (5). High j_x and low j_y current densities for
 2 in comparison with EPTA3 (Table 1) indicate
 significantly enhanced electrical conductivity along
 concurrent diminished conductivities along
 s higher anisotropy may be explained by the
 structure of PO342 (Fig. 1), which is charac-
 terized by elongated lenses of similar CPO parallel
 flow direction X (porphyroclasts or recryst-
 allized domains that had originated from a single
 oriented porphyroclast). These highly elongated
 roclasts correspond to grains in easy glide
 directions, characterized by $[1\ 0\ 0]$ semi-parallel
 shear direction (X). These lenses form thus a
 cted high-conductivity pathway along X and
 conductivity pathway along Y , resulting in a
 higher electrical anisotropy than the one that
 be produced by a similar CPO with a random
 orientation of the various CPO components.

FE electrical anisotropy calculated using MK90
 on data for 900A87 in the plane normal to the
 on (XZ) plane is more than twice as high as in
 w plane, XY (Fig. 4). Analysis of the current
 es reveals that the high anisotropy of 7.6 is
 by a high current density along X ($j_x = 0.528$)
 and a low current density along Z ($j_z = 0.069$).
 may be explained by the shape preferred ori-
 entation of large olivine porphyroclasts, like the one
 centre of the map (Fig. 1), which forms a
 uous olivine pathway with $[1\ 0\ 0]$ and $[0\ 1\ 0]$
 el to X and Z , respectively. For MK90 diffu-
 sivity data, this interconnected pathway enhances the
 t density along X because $[1\ 0\ 0]$ is the axis
 of highest conductivity. At the same time it blocks
 current along Z (y direction in the FEM model)
 $[0\ 1\ 0]$ is the direction of lowest conductiv-
 ity in the olivine crystal. In contrast, the anisotropy
 calculated in the XY plane (R-900A87 with
 a random microstructure as 900A87) is 3. The inter-
 connected porphyroclast pathway gives an almost

y direction of the FEM model. Since in the MK90
 data, $[0\ 0\ 1]$ has intermediate diffusivity values, this
 leads to an enhancement of the conductivity along
 the y direction of the FEM model resulting in a higher
 current ($j_y = 0.173$) and lower anisotropy in the flow
 plane. This effect is not observed for the models
 calculated using MK98 data, because of the lower
 anisotropy and smaller difference in olivine H^+ dif-
 fusivity between $[0\ 1\ 0]$ and $[0\ 0\ 1]$ directions.

Comparison between electrical conductivity anisotropy
 factor predicted by FEM models and random resistor net-
 works also suggests that both the CPO and microstruc-
 ture produced by plastic deformation in the mantle con-
 tribute to electrical anisotropy. Anisotropy factors calcu-
 lated of 100 random resistor networks range from <1 to
 15, i.e., maximum anisotropies similar to those predicted
 by FEM, but display an average value of 3 (Simpson and
 Tommasi, 2005). The present models suggest that orien-
 tation distributions producing high anisotropies are more
 common in deformed mantle rocks than those produc-
 ing low anisotropies. Thus, averaging a large number
 of random resistor networks tends to underestimate the
 actual electrical anisotropy factors that result from a
 given olivine CPO. The highest electrical anisotropy will
 be observed in samples in which dislocation glide pro-
 duced elongated grains even if these grains completely
 recrystallize, since these “fossil porphyroclasts” will still
 form elongated lenses with similar orientations, as in the
 experimentally deformed dunite PO342 (Bystricky et al.,
 2000). On the other hand, fast grain boundary migration
 during deformation will tend to hinder the development
 of highly elongated olivine grains, leading to a more ran-
 dom distribution of the most conductive orientations, like
 in sample EPTA3. Grain boundary migration is favored
 by high temperatures and low strain rates. The strongest
 anisotropy factors (>10) should thus occur in mantle
 rocks deformed under “lithospheric” conditions, i.e., at
 lower temperatures and/or high strain rates, in which
 grain boundary migration is limited.

5. Comparison of calculated electrical anisotropies with electromagnetic field studies data

Agreement between electrical and seismic anisotropy
 fast directions has been observed in many regions world-
 wide, like the Greenville belt in Canada (Ji et al., 1996;
 Sénéchal et al., 1996), the Appalachians (Wannamaker

uba, 2000), and central Germany (Leibecker et al., 2005; Gatzemeier and Moorkamp, 2005). How-
 anisotropy factors are only available for some of
 the samples. The observed anisotropies at the base of
 the samples vary between ~ 3 below central Australia,
 southern Bavaria, >35 for Fennoscandia and
 central Europe. The Fennoscandian data show
 abrupt changes of anisotropy in some areas
 due to variation of strike angle, Lahti et al., 2005) due
 to conductivity heterogeneities, which may have
 led to overestimation of the electrical anisotropy

of anisotropy factors ≤ 3 , like those observed
 in the northern or southeastern Brazil may easily be
 explained by an electrical conduction controlled by
 H^+ diffusion in the upper mantle. Indeed,
 the resistor network modelling of Simpson and
 2005) already showed that anisotropic H^+ dif-
 fusion in a textured peridotitic mantle can generate bulk
 anisotropies in the order of these observations. Finite-
 element modelling improves the prediction of electrical
 anisotropy compared to statistical/averaging schemes
 by taking into account the microstructure, spatial arrangement
 and connectivity of domains showing similar ori-
 entation. The present study shows that upper man-
 tle rocks showing typical high-temperature deformation
 structures and CPO will show electrical anisotropy
 ranging from 3 to 16, with the naturally deformed
 samples which were deformed at typical upper mantle
 conditions displaying a smaller range of anisotropy fac-
 tors (4 and 7).

Field studies mentioned above investigate the
 electrical anisotropy in a horizontal section at the base of
 the samples, i.e., in the asthenosphere. Mantle flow at
 asthenospheric depths is probably dominated by subhor-
 izontal shearing at low deviatoric stresses due to viscous
 drag in the asthenospheric mantle by the plate motion
 (e.g., 1998). Horizontal electrical anisotropies in
 the samples correspond to the “anisotropy within the
 plane” models indicated by (R-) in Table 1. For
 naturally deformed samples, using the KM98 diffu-
 sion coefficients the anisotropies in this plane are slightly lower
 than those in the plane normal to the shear zone and lie in a
 range between 4.0 and 5.0. The experimentally deformed
 samples show a significantly higher anisotropy (>15),
 whose microstructure of this sample should be less
 similar to those formed at asthenospheric condi-
 tions since it was formed at much higher strain rates
 and higher deviatoric stresses). Thus, although FEM predicts

and central Europe. Another conduction mechanism is
 required.

Besides partial melt, small amounts of highly conduc-
 tive phases like graphite (Duba and Shankland, 1982;
 Deines, 2002) and sulphides (e.g., Ducea and Park,
 2000) may enhance upper mantle conductivities if they
 form an interconnected network along grain boundaries.
 However, to produce a high electrical anisotropy, if the
 highly conductive phase is equally distributed along
 grain boundaries, a very strong shape preferred ori-
 entation is required in order to engender a significant
 enhancement of interconnectivity along the lineation
 (X direction in sample coordinate system) and concu-
 rent reduction of interconnectivity perpendicular to it (Y
 direction). Yet, as observed in sample EPTA3, under high
 temperature, low-stress conditions that are expected to
 prevail under asthenospheric depths, fast synkinematic
 grain boundary migration leads to development of weak
 shape preferred orientations.

Anisotropy could nevertheless be produced if the
 highly conductive phases were not evenly distributed
 along all grain boundaries. Analyses of the spatial
 arrangement of melt pockets in experimentally sheared
 peridotite + basalt assemblages (Holtzman et al., 2003)
 and of the crystallization of secondary clinopyroxenes in
 naturally deformed mantle rocks (Tommasi et al., 2004)
 suggests nevertheless that fluids tend to align in lens
 shaped pockets parallel or at low angle to the shear plane.
 In a subhorizontal shear zone, the highly conductive
 phases should therefore be concentrated in subhorizontal
 lenses and hence produce no anisotropy in long period
 MT data. In contrast, in a subvertical shear zone, e.g., a
 lithospheric strike slip fault, highly conductive aligned
 in the shear plane may add to the intrinsic anisotropy of
 olivine, resulting in strong electrical anisotropy.

A general outcome of the FEM results is that the
 weak anisotropy is not caused by low conductivities
 along the flow direction (X) but rather by high electri-
 cal conductivities perpendicular to it. From the calcu-
 lated current densities (Table 1), we may estimate the
 factor r_i , which is the electrical conductivity along a
 certain direction with respect to the electrical conduc-
 tivity along the olivine $[100]$ -axis. The samples with
 high anisotropy show for the high-conductivity direc-
 tion (j_x) a ratio r_x of about 0.45–0.55. The bulk electrical
 conductivity along that direction is therefore expected to
 be about half the intrinsic electrical conductivity along
 olivine $[100]$ -axis, $\sigma_{[100]}^{ol}$. Assuming saturated condi-
 tions (Lizarralde et al., 1995), H^+ diffusion can result

er and Moorkamp, 2005), Thus the extreme factors observed in this region imply a process hinder the conductivity in the N–S direction. Very different dominant conduction mecha-

Discussion

The finite-element modelling to quantify the anisotropy due to anisotropic intracrystalline diffusion in upper mantle rocks as a function of CPO and microstructure, which are described by orientation maps obtained by indexation of electron backscattered diffraction (EBSD) patterns. The studied peridotites have varied microstructures and olivine fabrics as a result of upper mantle deformation, with intensifying the entire range of CPO intensities usually observed in the upper mantle. Highest conductivity in the upper mantle is parallel to *X* direction, which is the flow direction as inferred from both the crystals elongation and the preferred orientation of olivine [100] crystallographic axes. The preferred orientation of the experimentally sheared dunite that shows a very strong anisotropy (>10), macroscopic electrical anisotropy factors range between 3 and 8. The magnitude of electrical anisotropy depends on a first order approximation of the olivine crystal preferred orientation. The relation saturates for strong crystal preferred orientations. Comparing the FEM results with models based on random resistor network modelling or averaging (e.g., VRH averages) shows that the distribution and, hence, the interconnectivity of the CPO components in mantle samples significantly influence their electrical anisotropy. These models provide a lower bound estimations of upper mantle anisotropies. The strongest anisotropy factors could occur in mantle rocks in which deformation-induced creep has produced not only crystal preferred orientations, even if the anisotropy is masked by recrystallization.

Low electrical conductivity anisotropy factors <10 , similarly inferred from MT data in Australia or Germany, may thus result from anisotropic H^+ diffusion in olivine in peridotites displaying olivine preferred orientations typical of upper mantle deformation. The anisotropy factors observed in other regions, like the East African Rift, imply that intracrystalline H^+ diffusion is the dominating conduction mechanism. However, the high anisotropies at asthenospheric depths could not be explained by the presence of aligned

simulations in combination with laboratory measurements of electrical conductivities on naturally deformed peridotites at high temperature and high water fugacity conditions are thus required to understand this data.

Acknowledgements

We thank Misha Bystricky, Walid Ben Ismail, and Emmanuela Pera for providing the EBSD maps of samples PO342, 900A87, and EPTA3, respectively. David Mainprice is thanked for stimulating discussions and for providing FORTRAN programs for treating the crystallographic orientation data and for calculating Voigt–Reuss–Hill averages of physical properties. A. Gatzemeier is funded by a post-doctoral scholarship from the Deutsche Forschungsgemeinschaft.

References

- Archie, G.E., 1942. The electrical resistivity log as an aid in determining some reservoir characteristics. *Trans. Am. Inst. Min. Metall. Petr. Eng.* 146, 54–62.
- Bahr, K., 1997. Electrical anisotropy and conductivity distribution functions of fractal random networks and of the crust: the scale effect of connectivity. *Geophys. J. Int.* 130, 649–660.
- Bahr, K., Dube, A., 2000. Is the asthenosphere electrically anisotropic? *Earth Planet. Sci. Lett.* 178, 87–95.
- Ben Ismail, W., Mainprice, D., 1998. An olivine fabric database: an overview of upper mantle fabrics and seismic anisotropy. *Tectonophysics* 296, 145–158.
- Bernasconi, J., 1974. Conduction in anisotropic disordered systems: effective-medium theory. *Phys. Rev. B* 9, 4575–4579.
- Bigalke, J., 1999. Investigation of the conductivity of random networks. *Physica A* 272, 281–293.
- Boullier, A.M., Nicolas, A., 1975. Classification of textures and fabrics of peridotites xenoliths from South African kimberlites. *Phys. Chem. Earth* 9, 467–475.
- Bunge, H.-J., 1982. *Texture Analysis in Materials Science*. Butterworth, London.
- Bystricky, M., Kunze, K., Burlini, L., Burg, J.-P., 2000. High shear strain of olivine aggregates: rheological and seismic consequences. *Science* 290, 1564–1567.
- Chelidze, T.L., Gueguén, Y., Ruffet, C., 1999. Electrical spectroscopy of porous rocks, a review—II. Experimental results and interpretation. *Geophys. J. Int.* 137, 16–34.
- Constable, S., Shankland, T.J., Dube, A., 1992. The electrical conductivity of an isotropic olivine mantle. *J. Geophys. Res.* 97, 2297–3404.
- Coverdale, R.T., Jennings, H.M., Garboczi, E.J., 1995. An improved model for simulating impedance spectroscopy. *Comp. Mat. Sci.* 3, 465–474.
- Deines, P., 2002. The carbon isotope geochemistry of mantle xenoliths. *Earth Sci. Rev.* 58, 247–278.
- Del Rio, J.A., Zimmerman, R.W., Dawe, R.A., 1998. Formula for the conductivity of a two-component material based on the reciprocity

- Shankland, T.J., 1982. Free carbon and electrical conduction in the earth's mantle. *Geophys. Res. Lett.*, 1271–1274.
- Park, S.K., 2000. Enhanced mantle conductivity from minerals, southern Sierra Nevada, California. *Geophys. Res. Lett.* 27, 2405–2408.
- Palciauskas, A.G., Ferguson, I.J., 2004. Lithospheric anisotropy inferred from collocated teleseismic and magnetotelluric data: Great Slave Lake shear zone, northern Canada. *Geophys. Res. Lett.* 31, L19614.
- Palciauskas, A.G., 1998. Finite element and finite difference programs for the linear electric and elastic properties of digital images of materials. NIST, Internal Report 6269.
- Palciauskas, A.G., Moorkamp, M., 2005. 3D modelling of electrical conductivity from electromagnetic array data: hypothesis testing for upper mantle conduction mechanisms. *Phys. Earth Planet. Inter.* 155, 215–242.
- Palciauskas, V., 1994. *Introduction to the Physics of the Earth's Interior*. Princeton University Press, Princeton, NJ.
- Palciauskas, V., 1962. A variational approach to the theory of the effective magnetic permeability of multiphase materials. *J. Geophys. Res.* 67, 3125–3131.
- Palciauskas, V., 1962. The elastic behaviour of a crystalline aggregate. *Proc. R. Soc. London A* 65, 349–354.
- Palciauskas, V., Chave, A., 2000. Comparison of continental and oceanic mantle electrical conductivity: is the Archean crust dry? *Geochem. Geophys. Geosyst.* 1: paper number 100048.
- Palciauskas, V., Kohlstedt, D.L., Zimmerman, M.E., Heidelbach, F., Hufstodt, J., 2003. Melt segregation and strain partitioning: implications for seismic anisotropy and mantle flow. *Science* 300, 1220–1223.
- Palciauskas, V., Mareschal, M., Senechal, G., 1996. Obliquity of seismic and electrical anisotropies as a potential indicator of recent sense for ductile shear zones in the upper mantle. *Geophys. Res. Lett.* 23, 1033–1036.
- Palciauskas, V., 1992. Water and graphite in the earth's crust – an alternative interpretation of conductivity models. *Surv. Geophys.* 7, 1–7.
- Palciauskas, V., 2000. The role of hydrogen in the electrical conductivity of the mantle. *Nature* 347, 272–273.
- Palciauskas, V., 1973. Percolation and Conduction. *Rev. Mod. Phys.* 45, 1–18.
- Palciauskas, V., Mackwell, S.J., 1998. Diffusion of hydrogen and point defects in olivine. *Zeitschrift für Physikalische Chemie* 202, 147–162.
- Palciauskas, V., 1999. Zwei- und dreidimensionale Widerstandsnetzwerkbeschreibung des Leitfähigkeitsmechanismus in der mittlen Kruste (in German). PhD Thesis. University of Göttingen, Germany.
- Palciauskas, V., Kaikkonen, P., Vaittinen, K., 2005. Decomposition of the BEAR magnetotelluric data: implications for the electrical conductivity in the Fennoscandian Shield. *Geophys. Res. Lett.* 32, 900–914.
- Palciauskas, V., 1952. The electrical resistance of binary metallic mixtures. *J. Appl. Phys.* 23, 779–784.
- Palciauskas, V., Gatzemeier, A., Höning, M., Kuras, O., Soyer, W., 2002. Models of electrical anisotropic structures in the lower crust and upper mantle beneath the Rhenish Shield. *Earth Planet. Sci. Lett.* 200, 1–12.
- Palciauskas, V., 1982. Seismic anisotropy in the upper mantle inferred from sounding using Hawaii-to-California submarine cable data. *J. Geophys. Res.* 87, 17837–17854.
- Mackwell, S.J., Kohlstedt, D.L., 1990. Diffusion of hydrogen in olivine: Implications for water in the mantle. *J. Geophys. Res.* 95, 5079–5088.
- Madden, T.R., 1976. Random networks and mixing laws. *Geophysics* 41, 1104–1125.
- Mainprice, D., Barruol, G., Ben Ismail, W., 2000. The seismic anisotropy of the Earth's mantle: from single crystal to polycrystal. In: Karato, S.I. (Ed.), *Earth's Deep Interior: Mineral Physics and Tomography from the Atomic to the Global Scale*. AGU, Washington, DC, pp. 237–264.
- Mainprice, D., Humbert, M., 1994. Methods of calculating petrophysical properties from lattice preferred orientation data. *Surv. Geophys.* 15, 575–592.
- Maxwell, J.C., 1881. *A Treatise on Electricity and Magnetism*, second ed. Clarendon, Oxford, England.
- Nicolais, A., Christensen, N.I., 1987. Formation of anisotropy in upper mantle peridotites – a review. In: Fuchs, K., Froidevaux, C. (Eds.), *Composition, Structure and Dynamics of the Lithosphere-Asthenosphere System*. AGU Geodynamics Series, vol. 16. American Geophysical Union, Washington, DC, pp. 111–123.
- Nye, J.F., 1985. *Physical Properties of Crystals: Their Representation by Tensors and Matrices*. Oxford University Press, Oxford, NY.
- Padilha, A.L., Vitorello, I., Padua, M.B., Bologna, M.S., 2006. Lithospheric and sublithospheric anisotropy beneath central-southeastern Brazil constrained by long period magnetotelluric data. *Phys. Earth Planet. Inter.* 158, 190–209.
- Reuss, A., 1929. Berechnung der Fließgrenze von Mischkristallen auf Grund der Plastizitätsbedingungen für Einkristalle. *Zeitschrift für angewandte Mathematik und Mechanik* 9, 49–58.
- Roberts, J.J., Tyburczy, J.A., 1999. Partial-melt electrical conductivity: Influence of melt composition. *J. Geophys. Res.* 104, 7055–7065.
- Sénéchal, G., Rondenay, S., Mareschal, M., Guilbert, J., Poupinet, G., 1996. Seismic and electrical anisotropies in the lithosphere across the Grenville Front, Canada. *Geophys. Res. Lett.* 23, 2255–2258.
- Schmelting, H., 1986. Numerical models on the influence of partial melt on elastic, anelastic and electrical properties of rocks. Part II: electrical conductivity. *Phys. Earth Planet. Inter.* 43, 123–136.
- Schulgasser, K., 1976. Relationship between single-crystal and polycrystal electrical conductivity. *J. Appl. Phys.* 47, 1880–1886.
- Shankland, T.J., Duba, A.G., 1990. Standard electrical conductivity of isotropic, homogeneous olivine in the temperature range 1200–1500°C. *Geophys. J. Int.* 103, 25–31.
- Shankland, T.J., Waff, H.S., 1977. Partial melting and conductivity anomalies in the upper mantle. *J. Geophys. Res.* 82, 5409–5417.
- Simpson, F., 2001. Resistance to mantle flow inferred from the electromagnetic strike of the Australian upper mantle. *Nature* 412, 632–635.
- Simpson, F., 2003. Intensity and direction of lattice-preferred orientation of olivine: are electrical and seismic anisotropies of the Australian mantle reconcilable? *Earth Planet. Sci. Lett.* 203, 535–547.
- Simpson, F., Tommasi, A., 2005. Hydrogen diffusivity and electrical anisotropy of a peridotite mantle. *Geophys. J. Int.* 160, 1092–1102.
- Stalder, R., Skogby, H., 2003. Hydrogen diffusion in natural and synthetic orthopyroxene. *Phys. Chem. Miner.* 30, 12–19.
- Stauffer, D., Aharony, A., 1992. *Introduction to Percolation Theory*. Taylor & Francis, London.

1998. Forward modeling of the development of seismic anisotropy in the upper mantle. *Earth Planet. Sci. Lett.* 160, 1–13.
- Gibert, B., Seipold, U., Mainprice, D., 2001. Anisotropy and diffusivity in the upper mantle. *Nature* 411, 783–786.
- Godard, M., Coromina, G., Dautria, J.M., Barszczus, H., 2001. Seismic anisotropy and compositionally-induced velocity variations in the lithosphere above mantle plumes: a petrological and structural study of mantle xenoliths from French Polynesia. *Earth Planet. Sci. Lett.* 227 (3–4), 539–556.
- Mainprice, D., Canova, G., Chastel, Y., 2000. Viscoplastic flow and equilibrium-based modelling of olivine lattice reorientations. Implications for upper mantle seismic anisotropy. *J. Geophys. Res.* 105, 7893–7908.
- Voigt, W., 1928. *Lehrbuch der Kristallphysik*. Teuber, Leipzig.
- Waff, H.S., 1974. Theoretical considerations of electrical conductivities in a partially molten mantle and implications for geothermometry. *J. Geophys. Res.* 79, 4003–4010.
- Wannamaker, P.E., et al., 1996. Magnetotelluric experiment probes deep physical state of southeastern U.S. *EOS* 77 (34), 329–333.
- Xu, Y., Shankland, T.J., Duba, A.G., 2000a. Pressure effect on electrical conductivity in the Earth's mantle. *Phys. Earth Planet. Int.* 118, 149–161.
- Xu, Y., Shankland, T.J., Poe, B.T., 2000b. Laboratory-based electrical conductivity in the Earth's mantle. *J. Geophys. Res.* 105, 27865–27875.